RESEARCH ARTICLE

ADVANCED FUNCTIONAL MATERIALS
www.afm-journal.de

Modulating the Hydrogenation Mechanism of Electrochemical CO_2 Reduction Using Ruthenium Atomic Species on Bismuth

Xiao Liu, Cheng Zhen, Junxiu Wu, Xiao You, Yudong Wu, Qi Hao, Gang Yu, M. Danny Gu, Kai Liu,* and Jun Lu**

The conversion of CO_2 into formate through electrochemical methods is emerging as an elegant approach for industrial-scale CO_2 utilization in the near future. Although Bismuth (Bi)-based materials have shown promise thank to their excellent selectivity, their limited reactivity remains a challenge. Herein, this study demonstrates a significant enhancement in the CO_2-to-formate efficiency of Bi by incorporating ruthenium (Ru) atomic species. Ru single atom doped Bi exhibited a nearly twofold higher partial current density compared with pure Bi and Ru clusters doped Bi, while over 95% Faradaic efficiency (FE) is maintained. Through comprehensive investigations using a combined approach of electrochemical techniques, operando spectroscopy, and theoretical calculations, this study elucidates that the presence of Ru single atom promotes H_2O dissociation and H* migration to Bi sites for CO_2-to-formate conversion by significantly reducing the energy barrier via a H* spillover path. Besides, it is constructed Ru–Bi bridge sites for efficient CO_2 hydrogenation via a non-spillover path, which served as the major mechanism for CO_2-to-formate conversion in Ru single atom doped Bi.

1. Introduction

CO_2 capture from point or diluted sources, combined with subsequent electrochemical reduction (CO_2RR) using renewable energy, offers an attractive approach to produce high value chemicals while mitigating greenhouse gas emission at the same time.[1] Among various chemicals that can be obtained via CO_2RR, formate is particularly attractive due to high energy density, and its potential use as chemical fuel.[2] In addition, CO_2-to-formate conversion is widely regarded as one of the most probable process to achieve industrialization amongst various CO_2RR processes due to high energy efficiency and selectivity.[3] As the result, tremendous efforts have been dedicated to develop high performance CO_2RR catalysts to produce formate. Among various catalysts

---

X. Liu
College of Environmental and Resource Sciences
Zhejiang University
Hangzhou, Zhejiang 310058, China

X. Liu, Y. Wu, Q. Hao, K. Liu
Key Laboratory of Coastal Environment and Resources of Zhejiang Province
School of Engineering
Westlake University
Hangzhou, Zhejiang 310030, China
E-mail: liukai@westlake.edu.cn

C. Zhen
Department of Materials Science and Engineering
Southern University of Science and Technology
Shenzhen 518055, China

J. Wu, J. Lu
College of Chemical and Biological Engineering
Zhejiang University
Hangzhou, Zhejiang 310027, China
E-mail: junzoelu@zju.edu.cn

X. You
Center of Synthetic Biology and Integrated Bioengineering
School of Engineering
Westlake University
Hangzhou, Zhejiang 310030, China

G. Yu
Advanced Interdisciplinary Institute of Environment and Ecology
Guangdong Provincial Key Laboratory of Wastewater Information Analysis and Early Warning
Beijing Normal University
Zhuhai 519087, China

M. D. Gu
Eastern Institute for Advanced Study
Eastern Institute of Technology
Ningbo, Zhejiang 315200, China
E-mail: mgu@eitech.edu.cn

The ORCID identification number(s) for the author(s) of this article can be found under https://doi.org/10.1002/adfm.202405835

DOI: 10.1002/adfm.202405835

reported, main group metal elements, including Sn,[4] In,[5] and Bi,[6] have demonstrated high reactivity and selectivity toward CO_2-to-formate conversion. In particular, Bi-based catalysts attract much attention due to their superior ability to adsorb CO_2 and to form HCOO* intermediate, both are essential for formate formation.[7]

For CO_2-to-formate catalyzed by Bi-based catalysts, it is well-established that the first proton-coupled electron transfer (PCET) is the rate-determining step (RDS).[8] Thus, over past years, researchers have extensively focused on the reduction of the energy barrier for this step, primarily via the optimization of the electronic structure of Bi-based catalysts. However, recently it was reported that an alternative step maybe responsible for the efficient CO_2-to-formate process. More specifically, reactive hydrogen (H*) is first generated at active sites for Volmer step, followed by migration to adjacent active sites to form HCOO* intermediates (Equations 1 and 2).[9] Unfortunately, for Bi-based catalysts, hydrogen evolution reaction (HER) is usually suppressed and large applied potentials are needed to generate H* to drive the CO_2RR at the expense of charge utilization efficiency.[10] Furthermore, undesired Heyrovsky step may occur if H* cannot migrate immediately to the CO_2RR site.

$$H_2O + \mathrm{M} + e^- \rightarrow \mathrm{M} - H^* + \mathrm{OH}^- \tag{1}$$

$$^* + CO_2 + H^* \rightarrow {}^* + \mathrm{HCOO}^* \tag{2}$$

Therefore, it can be expected that efficient H_2O dissociation and H* spillover at more positively applied potentials can greatly promote CO_2-to-formate electrochemically. In fact, previously sulfur species have been reported to facilitate such process by lowering the H_2O activation potential.[9] Besides, noble metal possesses excellent hydrogen adsorption–desorption features. It has been reported that when Ag nanoparticles were added to bismuth subcarbonate nanosheet array, significant improvement in CO_2-to-formate conversion was observed due to accelerated H_2O dissociation and H* spillover.[11] During H* spillover, H* is migrated from water splitting site on Ag nanoparticles to the substrate, and continues to migrate on the substrate until it is reacted. However, along the migration path, H_2 production from H* recombination (via Tafel step) or reaction with water (via Heyrovsky step) may be expected. In this case, reducing the size of nanoparticles to clusters or even single atoms is a promising strategy to improve atom utilization, as well as shorten or even eliminate the H* migration path, which can reduce the undesired HER.

With this understanding, within the current study, we employed Ru doped Bi as a model system, as Ru is known to exhibit excellent hydrogen adsorption–desorption features.[12] CO_2-to-formate conversion efficiency was evaluated as a function of Ru species. We found Ru single atom doped Bi achieves about twofold higher CO_2-to-formate reactivity in comparison to pure Bi and Ru cluster doped Bi, and high Faradaic efficiency (FE) of formate (>93%) can be maintained over a wide range of applied potential from −0.8 to −1.2 V versus RHE. A combined approach of electrochemical techniques, operando spectroscopy, and theoretical calculations revealed in addition to the existing H* spillover mechanism, Ru single atom doped Bi facilitated CO_2-to-formate conversion by enabling CO_2 hydrogenation at Ru–Bi bridge sites, thus mitigates HER. Our finding is important for the designing of high performance electrocatalytic systems, especially for those that involves hydrogenation as RDS.

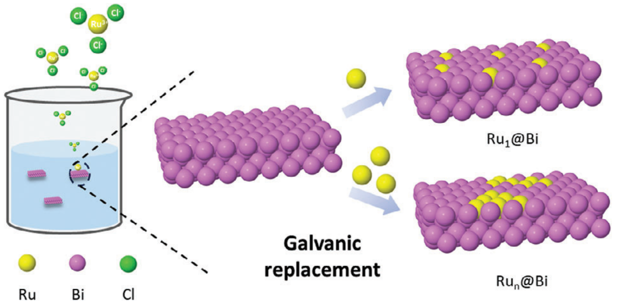

Scheme 1. Schematic representation of the preparation of catalysts.

2. Results and Discussion

2.1. Characterization

The typical synthetic route via galvanic replacement is shown in **Scheme** 1 (see the Experimental Section for details). The Ru doped Bi samples with different Ru loading contents were prepared by varying the volume of ruthenium chloride ($RuCl_3$) solution. The Ru loading contents, measured by inductively coupled plasma mass spectrometry (ICP-MS), were shown in Table S1 (Supporting Information). Ru single atoms and Ru clusters supported by Bi are denoted as Ru_1@Bi (with 0.6 wt.% Ru content) and Ru_n@Bi (with 1.2 wt.% Ru content), respectively.

The crystal structure of all samples was analyzed by X-ray diffraction (XRD). As depicted in Figure S1 (Supporting Information), Ru_1@Bi and Ru_n@Bi shared similar XRD pattern with Bi substrate, exhibiting a typical rhombohedral crystal structure of Bi (JCPDs#44-1246), which did not reveal significant structural variations. This can be attributed to the small feature size of the Ru species deposited on the surface. It is worth noting that a small but broad diffraction peak at ≈32° can be observed. This peak may be ascribed to Bi_2O_3 (JCPDS 45-1344), consistent with previous reports that metallic Bi is prone to oxidation in the ambient environment.[13]

All samples shared similar morphology as observed by transmission electron microscopy (TEM) as shown in Figure S2 (Supporting Information). Aberration-corrected high-angle annular dark-field scanning transmission electron microscopy (AC-HAADF-STEM) image of Bi was collected (Figure S3a, Supporting Information), which displays lattice fringes corresponding to (110) planes of the rhombohedral Bi crystal in accordance with XRD results. The fast Fourier transform (FFT) pattern also confirmed the [001] zone axis for the pure Bi (Figure S3b, Supporting Information). In addition, AC-HAADF-STEM revealed that the Bi substrate for Ru_1@Bi (**Figure** 1a) demonstrated dominant orientation of crystal facet with 0.332 nm distance, which can be assigned to (012) facet of rhombohedral Bi crystal (Figure 1b insert). Furthermore, the characteristic lattice distance of 0.279 nm can be ascribed to (200) facet of Bi_2O_3 (Figure S4, Supporting Information), it confirms the existence of Bi_2O_3 in the as-prepared Ru_1@Bi and Ru_n@Bi samples. Although, it has to be noted that

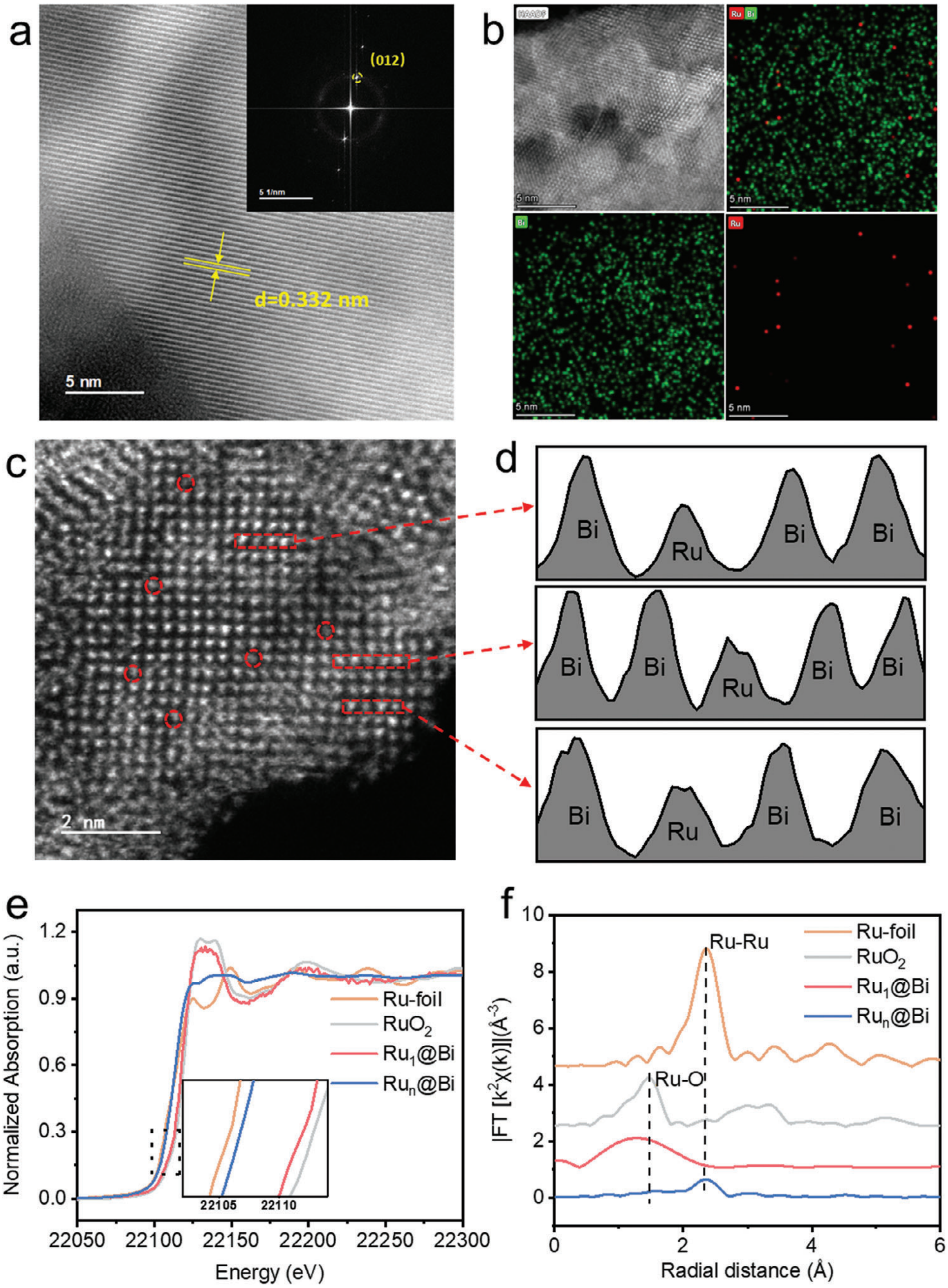

Figure 1. Structural characterization of the catalysts. a) AC-HAADF-STEM image of the Ru$_1$@Bi and corresponding FFT pattern (insert). b) EDS mapping images (green: Bi element; red: Ru element) and c) Atomic-resolution AC-HAADF-STEM image of Ru$_1$@Bi. d) Intensity profiles of Ru single atoms in Figure 1c; e) The normalized XANE spectra at Ru K-edge; f) The k^2-weighted FT-EXAFS in R-space, along with the spectra of Ru foil and RuO$_2$ as reference.

the peaks responding to Bi–O stretches[8a] were disappeared during the CO$_2$RR process according to in situ Raman spectroscopy (Figure S5, Supporting Information).

For Ru$_1$@Bi, AC-HAADF-STEM combined with energy dispersive spectroscopy (EDS) mapping revealed that Ru atoms are well dispersed on Bi substrate as shown in Figure 1b and no segregation of Ru atoms are observed. We then employed atomic resolution AC-HAADF-STEM to further distinguish Ru atoms from the Bi support based on contrast difference. As shown in Figure 1c, darker dots and atom-sized features suspected to attribute to individual Ru atoms can be discerned on the surface of Ru$_1$@Bi. Note that the contrast difference between Ru and Bi atoms is subtle, therefore intensity profiles at various regions (Figure 1d) were used to demonstrate the existence of possible Ru single atoms. In contrast, the adjacent bright Ru element mapping spots in EDS mapping of Ru$_n$@Bi (Figure S6, Supporting Information) are suspected to be Ru clusters.[14]

To further probe the chemical state and local coordination environment of the Ru atoms in Ru_1@Bi and Ru_n@Bi, we performed X-ray adsorption spectroscopy (XAS), including X-ray absorption near edge structure (XANES) and extended X-ray absorption fine structure (EXAFS) measurements. The Ru K-edge XANES spectrum of Ru_1@Bi and Ru_n@Bi are located between those of Ru foil and RuO_2 reference sample (Figure 1f), illustrating the oxidation states of Ru atoms in Ru_1@Bi and Ru_n@Bi were $+\delta$ and $+\epsilon$ ($0 < \epsilon < \delta < 3$), respectively. The presence of oxidized Ru species can be attributed to sample oxidation due to exposure of the ambient environment.[15] During the subsequent CO_2RR test, the applied potentials were much lower than the standard reduction potential of Ru^{3+}/Ru (0.6 V vs RHE), thus we expect that the oxide cannot be retained and the main form of Ru in the working catalyst is Ru^0. Fourier-transformed (FT) EXAFS spectra are shown in Figure 1g, the k^2-weighted FT-EXAFS curve of the Ru_1@Bi shows a peak at ≈1.53 Å which is attributed to Ru—O bond, in accordance with the XANES results. Note that no Ru—Ru bonds were detected, verifying the presence of solely atomically dispersed Ru atoms. Whereas, for Ru_n@Bi, a peak ≈2.40 Å can be assigned to Ru—Ru bond scattering, confirming the existence of Ru clusters. Therefore, combine the above results, we have demonstrated that isolated Ru single atoms and clusters were successful immobilized on the Bi substrate of Ru_1@Bi and Ru_n@Bi, respectively.

2.2. Performance

To investigate the CO_2RR performance of the electrocatalysts, we first recorded linear sweep voltammograms (LSV) as depicted in **Figure 2a**. In Ar-saturated electrolyte, both Ru_1@Bi and Ru_n@Bi samples exhibit enhanced current densities for the HER in comparison to that of pure Bi. The current density increases with the Ru content, demonstrating the acceleration of H_2O dissociation. In comparison, in CO_2-saturated electrolyte, the onset potential of all samples shifted to a more positive value and the current density increased obviously, indicating that the catalysts strongly favor the CO_2RR over the HER. Not surprisingly, the current density increases with the Ru content too, demonstrating enhanced CO_2RR kinetics. The catalytic performance at different cathodic potentials between −0.70 and −1.3 V (all potentials are referenced to the reversible hydrogen electrode (RHE)) were investigated, and the resultant potential-dependent FE bar graph was shown in Figure 2b. The FE of Ru_1@Bi was not obviously improved compared with pure Bi, which is already high enough (maintained at >90% from −0.7 to −1.2 V). Intriguingly, though Ru_n@Bi displayed the highest reaction rate, its FE was much lower than other catalysts. The partial current density for formate production can provide a more accurate comparison of CO_2-to-formate performance of these electrocatalysts. Our results confirmed that Ru_1@Bi displayed the highest performance amongst three electrocatalysts between −0.70 and −1.2 V (Figure 2c), about twofold higher in partial current density compared with pure Bi and Ru_n@Bi. These results provide solid evidence that when Ru species are properly interfaced with Bi substrate, appropriate synergy between Ru and Bi may significantly impact the HER versus CO_2-to-formate selectivity. It is obvious that when Ru species exists in the form of cluster, pronounced HER was observed. In addition, it remains challenging to completely inhibit HER at very low applied potential (−1.3 V) due to H* dimerizing or reacting with H_2O. Since Ru_1@Bi displayed the highest performance, the durability was examined via *i*–*t* test, both current density and formate FE were largely maintained after 24 h of continuous electrolysis without the need of additional overpotentials (Figure 2d). Indeed, XRD patterns of Ru_1@Bi did not reveal any change upon the CO_2RR tests (Figure S7, Supporting Information). These results demonstrate the high stability of Ru_1@Bi under the reaction conditions. Overall, such high j_{HCOO-} obtained from Ru_1@Bi ranks among the highest levels of CO_2-to-formate performance of reported Bi-based electrocatalysts, as summarized in Figure 2e and Table S2 (Supporting Information).

2.3. Mechanism

Ru_1@Bi has shown a remarkable improvement in CO_2-to-formate performance at a wide range of applied potentials over pure Bi and Ru_n@Bi (Figure 2c). Therefore, it is imperative for us to understand the origin of such improvement. To rule out the possibility that the increased CO_2RR performance is due to variations in conductivity, and difference in concentration of active sites of these electrocatalysts, we performed the following experiments. We first compared the double-layer capacitance (C_{dl}) of the electrocatalysts to estimate the electrochemical surface area (ECSA) as shown in Figure S8 (Supporting Information). We observed the C_{dl} values are 4.20, 4.37, and 3.97 $\mu F \cdot cm^{-2}$ for pure Bi, Ru_1@Bi, and Ru_n@Bi. Such negligible variations in C_{dl} values can be explained by the low concentration of Ru species doped on Bi support, which does not significantly alter the number of exposed active sites. Thus, Ru_1@Bi still exhibited higher current densities for formate after corrected with ECSA (Figure S9, Supporting Information). Besides, the difference in CO_2-to-formate performance may also arise from charge transfer resistance. To this end, the Nyquist plots of the electrochemical impedance spectroscopy (EIS) were conducted in CO_2 saturated $KHCO_3$ electrolyte (Figure S10, Supporting Information). Both Ru_1@Bi and Ru_n@Bi have comparable semicircle diameter in the Nyquist plot, suggesting similar charge transfer resistance (R_{ct}). In contrast, pure Bi exhibits slightly greater semicircle diameter, indicating that the loading of Ru does not significantly improve the charge transfer property of the catalyst, which is not the decisive factor for performance improvement.

Previous works have demonstrated that H_2O dissociation is a slow step for the CO_2RR in alkaline and neutral media.[9a] Therefore, we speculate that the enhanced CO_2RR performance of Ru_1@Bi may be related to the promoted H_2O dissociation on Ru to supply H* species. This can be verified by the kinetic isotope effect (KIE) of H/D,[16] which was defined as the ratio of formate productivity in H_2O and D_2O. As shown in **Figure 3a**, the KIE values of H/D in CO_2RR to formate were calculated to be 1.93, 1.26, and 1.17 for pure Bi, Ru_1@Bi, and Ru_n@Bi, respectively. The KIE value for pure Bi is characteristic of primary KIE, suggesting H_2O dissociation was involved in the RDS for the CO_2RR-to-formate over pure Bi. However, since the introduction of Ru, the KIE value dropped to ≈1, which suggests that H_2O dissociation step is no longer related to RDS.

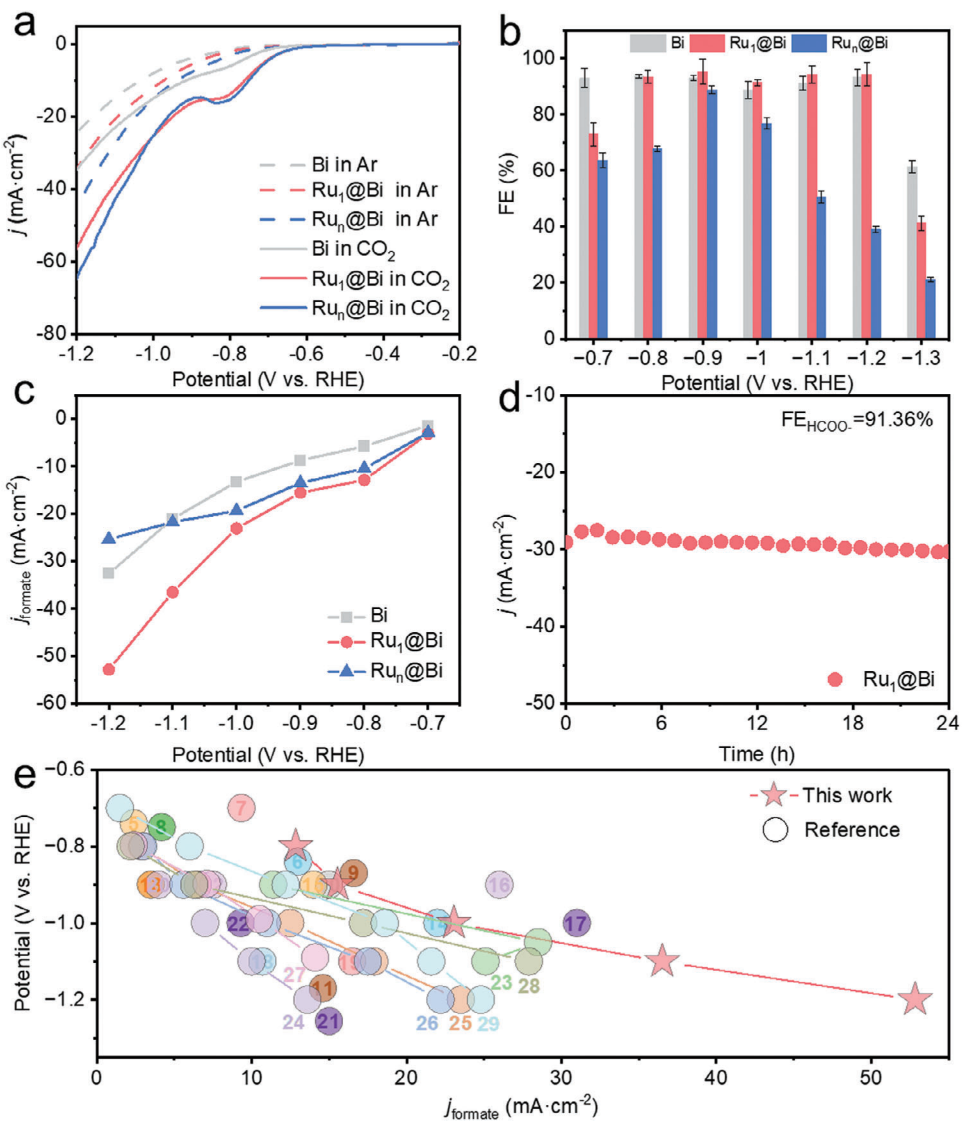

Figure 2. a) LSV polarization curve for CO_2RR in CO_2-saturated 0.5 м $KHCO_3$. b) Comparison of formate FE at various applied potentials. The FEs of the products were taken after 30 min electrolysis. c) Partial current densities for formate of prepared catalysts. d) Durability via *i*–*t* test of Ru1@Bi in the H-cell configuration for 24 h at −1.0 V. e) CO2RR performance in H-cell systems comparison with reported data in the literature (The inserted reference numbers represent the references in Table S2, Supporting Information).

Furthermore, we examined the generation of H* qualitatively using trapping experiment. The enhanced H* generation was verified by the addition of tertiary butanol (t-BuOH) in the electrolyte, which was reported to trap H* species.[17] As shown in Figure 3b, the CO_2RR current was decreased for all catalysts after the addition of t-BuOH. When a low concentration of t-BuOH was added (0.1 м), the amount of reduction in current densities were very close for these three catalysts, suggesting that the generated H* was only partially trapped by t-BuOH. When higher concentrations of t-BuOH (2.5 м) were introduced, a larger decay of current density was observed over Ru_1@Bi and Ru_n@Bi in comparison with pure Bi, indicative of the higher concentration of H* promoted by Ru species. It has to be noted that quantitative approaches, when available, are needed to further investigate the formation of H*.

In addition to H* generation, H* spillover is also responsible for the CO_2 hydrogenation to form HCOO*,[9] which is a key intermediate in CO_2-to-formate process. We then speculate that the superior CO_2-to-formate performance observed on Ru_1@Bi over Ru_n@Bi maybe due to the enhanced ability of H* spillover. To this end, cyclic voltammetry (CV) measurements were carried out. As shown in Figure 3c, the CV curves of Bi exhibit a reduction peak at ≈0.2 V in the cathodic direction and an oxidation wave at ≈0.6 V in the anodic direction, which are attributed to the reduction of oxidized Bi to its metallic form, and its reoxidation on the surface of the catalyst.[6a] In the anodic direction, a small oxidation peak was observed at ≈0.45 V before the oxidation peak of Bi, which can be attributed to the desorption of H*.[18] The peak area of H* desorption peak appears to increase with increasing Ru contents, indicating that Ru can significantly

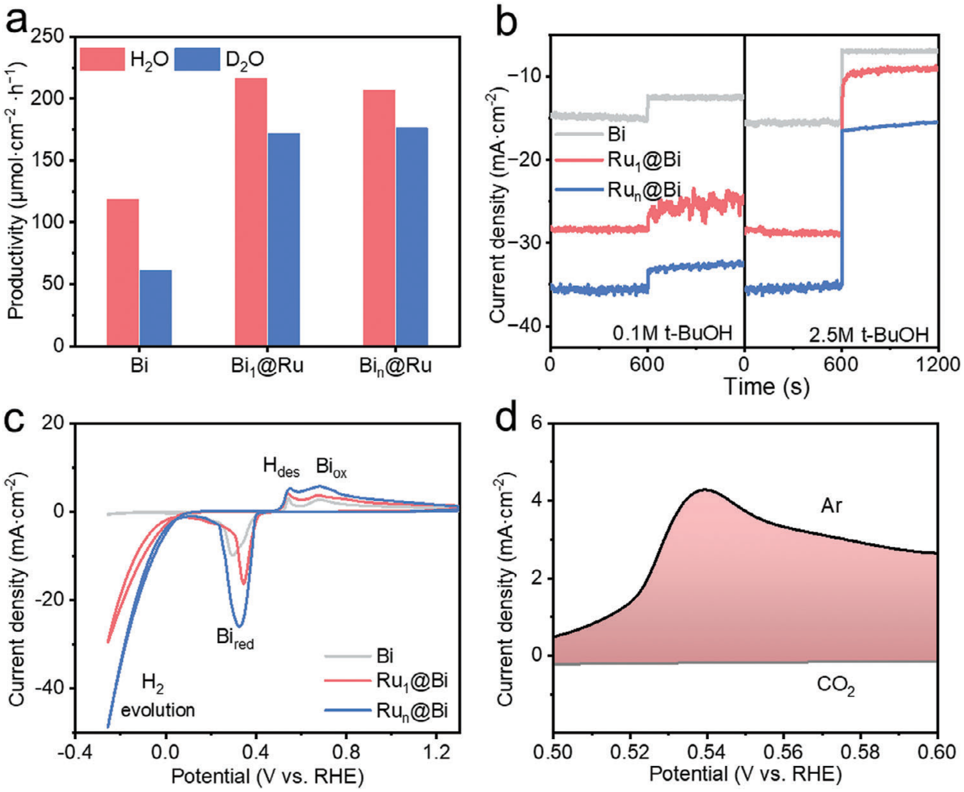

Figure 3. a) Comparison of the formate productivity over different catalysts in CO_2-saturated $KHCO_3-H_2O$ solution and a CO_2-saturated $KHCO_3D_2O$ solution. b) *I*–*t* curves of different catalysts at −1.0 V in a CO_2-saturated 0.5 M $KHCO_3$ solution with different concentrations of t-BuOH. c) CV curves of different catalysts in Ar-saturated 1 M KOH solution with a scan rate of 10 mV·s^{-1}. d) CV curves of Ru_1@Bi in Ar-saturated and CO_2-saturated 1 M KOH solution with a scan rate of 10 mV·s^{-1}.

increase the concentration of H*. Besides, the H* desorption peak of Ru_1@Bi disappeared with the addition of CO_2 (Figure 3d), suggesting that the migrated H* may react with CO_2. In addition, compared with pure Bi, a positive shift of Bi reduction peak was observed for Ru_1@Bi (Figure 3c), suggesting the H* may migrate from Ru to Bi and act as a reducing agent to facilitate Bi reduction. Compared with Ru_1@Bi, the Bi reduction peak for Ru_n@Bi exhibited a negative shift, indicative of hindered H* migration, which is consistent with our initial hypothesis. This can be attributed to higher energy barrier for H* migration according to our DFT results (Figures S11 and S12, Supporting Information).

2.4. ATR-SEIRAS and DFT Calculations

To further probe the catalytic intermediates, in situ attenuated total reflection-surface enhanced infrared absorption spectroscopy (ATR-SEIRAS) was employed to characterize the reaction species over pure Bi, Ru_1@Bi, and Ru_n@Bi. **Figure** 4a,b, and c revealed variations in several distinct infrared bands observed while sweeping the potentials from −0.2 to −1.3 V. The bands ≈1613–1650 and 1400 cm^{-1} correspond to OH bending vibration (δ(OH)) of H_2O* and symmetric OCO stretches (v_s(OCO)) of HCOO*, respectively.[5b,19] In order to assess the evolution of catalytic intermediates at different applied potentials, we integrated the peak areas of these IR peaks (Figure 4d,e).

For pure Bi, H_2O* showed a positive band, and the peak area steadily increased from −0.2 to −1.3 V (Figure 4a,d). This suggests a gradual accumulation of H_2O molecules on the surface of pure Bi, which is consistent with its poor ability of H_2O dissociation. A similar trend was observed for Ru_1@Bi in the range from −0.2 to −0.8 V, but a plateaued region can be observed at more negative potentials (Figure 4b,d). We speculate that a matched rate of H_2O dissociation and CO_2 hydrogenation to form HCOO* are responsible for this region. However, the peak aera of H_2O* rapidly dropped when the potential was decreased to −1.3 V, which is consistent with the pronounced HER (Figure 2b). In contrast, sunken peak of H_2O* was observed for Ru_n@Bi (Figure 4c,d), suggesting rapid consumption of H_2O*,[20] which confirms that the introduction of Ru cluster can greatly promote H_2O dissociation. Unfortunately, competitive HER took place at these conditions, leading to a decreased selectivity of CO_2RR (Figure 2b).

On the other hand, HCOO* is considered as a key intermediate for CO_2-to-formate. For pure Bi, the peak area of HCOO* gradually accumulated after −0.8 V (Figure 4a,e), while similar trend can be observed at much higher potentials for Ru_1@Bi and Ru_n@Bi (Figure 4b,c,e). This observation agrees well with our LSV result (Figure 2a) where the onset potential shifted to a more positive value after the introduction of Ru species. It's

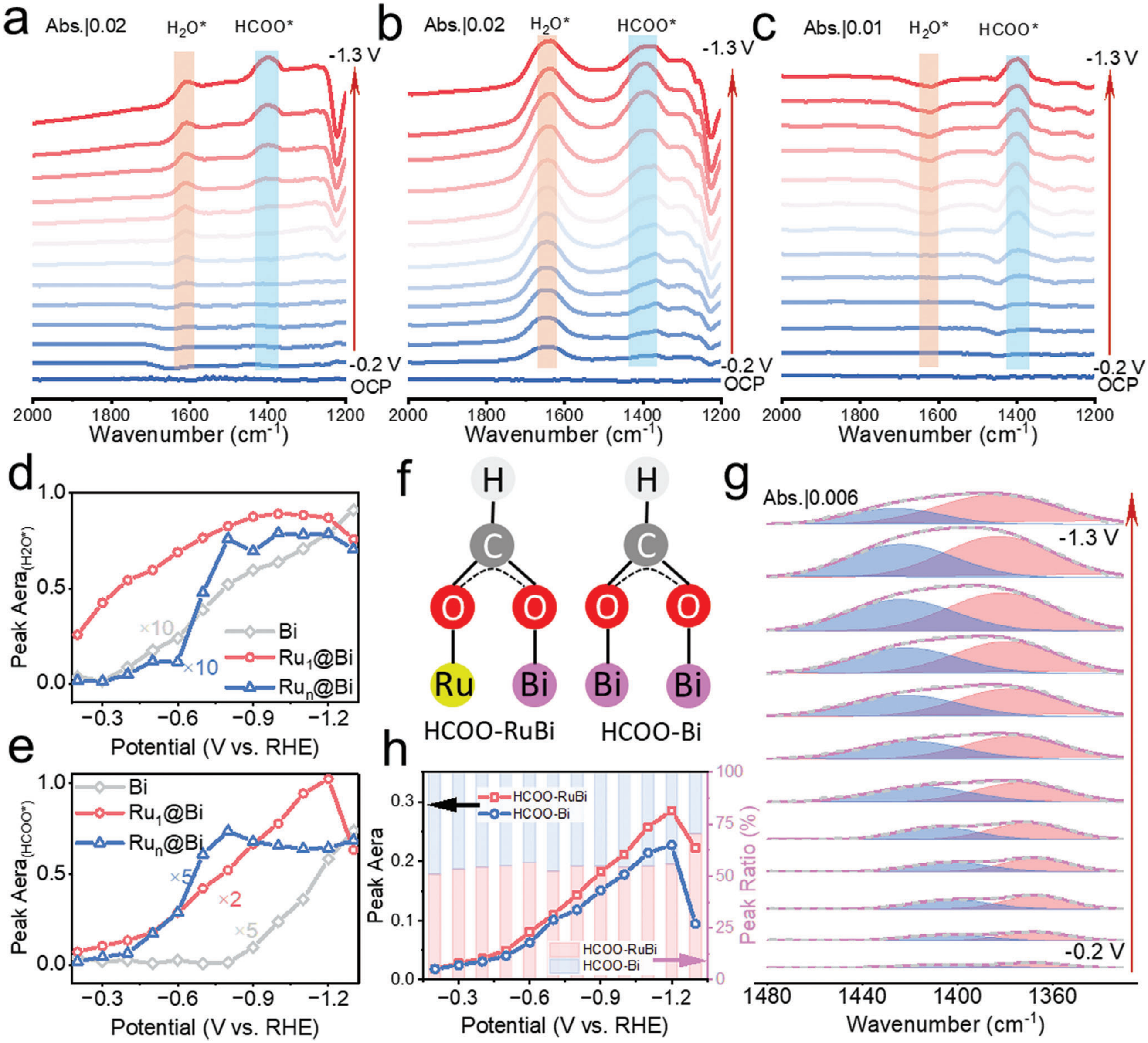

Figure 4. In situ ATR-SEIRAS obtained during LSV in a potential range from −0.2 to −1.3 V versus RHE for a) Bi, b) Ru_1@Bi, and c) Ru_n@Bi, highlighting peaks associated with intermediate species H_2O^* and HCOO*. Potential-dependent integrated peak aera plot for d) H_2O^* and e) HCOO* derived from Figure 4a,b,c. f) Schematic illustration of coordination modes of HCOO* at Ru–Bi bridge site and Bi–Bi site. g) Gaussian fitting of HCOO* IR peak for Ru_1@Bi, red represents HCOO*-RuBi, blue represents HCOO*-Bi. h) Potential-dependent integrated peak aera and peak ratio plot of HCOO*-RuBi and HCOO*-Bi peaks from Figure 4g.

worth nothing that for Ru_1@Bi, the peak area of HCOO* steadily increased, suggesting the accumulation of formate. In contrast, the peak of HCOO* for Ru_n@Bi remained largely unchanged between applied potential of −0.8–−1.2 V. Since concentration of HCOO* was unchanged, increase in overall reaction rate can be attributed to the increase of competitive HER. In summary, based on the above analysis, we conclude that efficient water dissociation by Ru species contributes to the improved performance of CO_2RR-to-formate, and Ru_1@Bi outperformed Ru_n@Bi due to balanced water dissociation and CO_2 hydrogenation rate.

It is possible that for Ru species, water dissociation and CO_2 hydrogenation may occur by a H* spillover path, where the former occurs on Ru species and the latter occurs on Bi; or via a non-spillover path where they may occur simultaneously on Ru species. DFT calculations were implemented to evaluate both scenarios and our results are summarized in Figures S11 and S12 (Supporting Information) for Ru_1@Bi and Ru_n@Bi, respectively. The relaxed possible structures of reaction intermediate on Ru_1@Bi and Ru_n@Bi substrate (Bi(001)) and corresponded total energy are displayed in Figures S13 and S14 (Supporting Information). We found Ru_1@Bi favors non-spillover

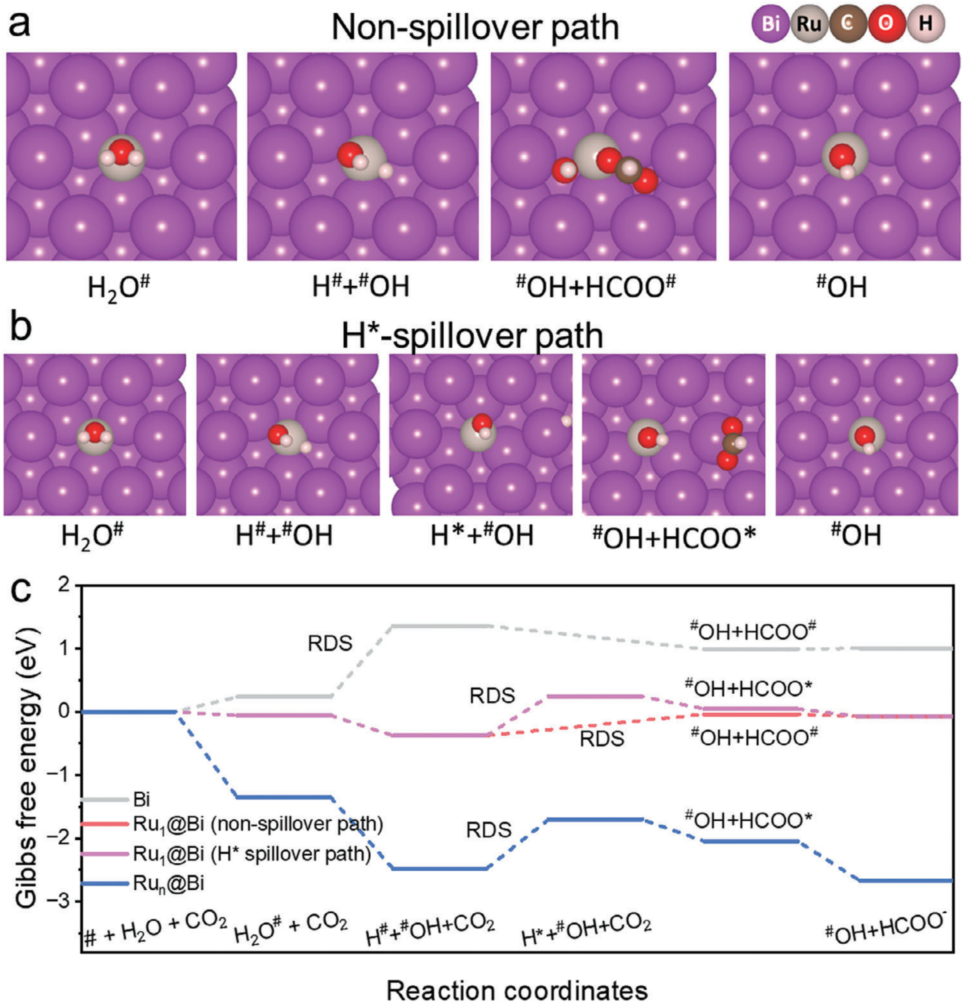

Figure 5. Optimized geometries for a) non-spillover path and b) H* spillover path of CO_2-to-formate mechanism on Ru_1@Bi. # and * denote the support and are used to distinguish differences in reaction sites. The optimized geometries for the reaction intermediates are also displayed with the color of elements labeled. c) Gibbs free energy landscapes for CO_2 reduction to formate at 0 V versus RHE. The RDS is labeled with a black text.

path, since the H* spillover path exhibited higher energy barrier (0.620 eV) (Figure S11, Supporting Information). More specifically, H* tends to drift toward the edge of Ru–Bi, where it participates in the hydrogenation CO_2 to form Ru–Bi bridged HCOO* intermediate. In contrast, we found that Ru_n@Bi favors the hydrogen spillover path, which has lower energy barrier compared to that of non-spillover path (Figure S12, Supporting Information). In other words, the preferential coordination mode of HCOO* was HCOO-RuBi and HCOO-Bi as illustrated in Figure 4f, for Ru_1@Bi and Ru_n@Bi, respectively.

In order to gain additional experimental evidence, we deconvoluted the IR peak of HCOO* from in situ ATR-SEIRAS to search for evidence of difference in coordination environment. For Ru_1@Bi, we found the IR peak of HCOO* appears to be broad and asymmetrical compared to that of Ru_n@Bi and Bi (Figure 4b). Gaussian fitting shows that the HCOO* stretching band can be resolved into two distinct components (Figure 4g). The wavenumber ≈1404–1426 cm^{-1} is rather close to ν_s(OCO) of pure Bi and Ru_n@Bi, suggesting similar coordination environment. For the lower wavenumber (1365–1383 cm^{-1}), we suspected that the red shifts are due to a different coordination environment. Therefore, to validate our hypothesis, the electron transfer and configuration was analyzed by optimized structure of HCOO* adsorption Ru_1@Bi and Ru_n@Bi, since which can represent the HCOO-RuBi and HCOO-Bi coordination mode, respectively. We found the charge transfer from Ru_1@Bi support to HCOO* is lesser than that of Ru_n@Bi according to Bader charges, leading to lower charge density of the OCO double bond (Figure S15, Supporting Information). It is known that decrease in charge density generally result in the red shift of the IR spectra. In addition, DFT calculations based on the Blyholder model show that the binding energy of HCOO* is lower at Ru–Bi bridge site compared to Bi site (Figure S16, Supporting Information), which leads to the red shift of the HCOO* vibration frequency.[21] Hence, we can reasonably infer that the bands ≈1404–1426 and 1365–1383 cm^{-1} can be assigned to HCOO* adsorbed on Bi and Ru–Bi bridge site, respectively. We further analyzed the potential dependent integrated peak area and ratio of HCOO-RuBi and HCOO-Bi (Figure 4h). Results show that the peak areas of HCOO-RuBi were consistently higher than that of HCOO-Bi at all applied potentials, which imply that non-spillover path is the major mechanism for $Ru_1@Bi$, and H* spillover path is the minor mechanism. This result is consistent with our DFT calculation, which shows that CO_2 hydrogenation at Ru–Bi bridge site was favored due to lower energy barrier.

Based on the above analysis, we summarized the optimal reaction path of CO_2-to-formate conversation and the optimized geometries are illustrated in **Figure** 5a,b, and Figure S17 (Supporting Information). Gibbs free energy (ΔG) landscapes in Figure 5c and the values of ΔG were listed in Table S4 (Supporting Information). As is shown in Figure 5c, for pure Bi, the Volmer step is the RDS with an energy barrier of +1.126 eV. After introduction of Ru species, it became exothermic with ΔG equals to −0.32 eV for $Ru_1@Bi$ and −1.128 eV for $Ru_n@Bi$. That is to say, the introduction of Ru on Bi shifts the active site for the Volmer step from Bi to Ru, facilitating generation of H*. For $Ru_1@Bi$, non-spillover path is the dominating CO_2-to-formate mechanism, with HCOO* formation as the RDS with energy barrier of +0.337 eV. H* spillover path is the minor mechanism, by which H* migration is the RDS with energy barrier of +0.620 V. It has to be noted that, the energy barrier of H* migration for $Ru_1@Bi$ is lower than that of $Ru_n@Bi$ (+0.771 eV), certified of facilitated H* migration. On the other hand, compared with $Ru_1@Bi$, $Ru_n@Bi$ favors HER and are more prone to *OH poisoning due to lower energy barrier (Figure S18 and Table S5, Supporting Information).

3. Conclusion

In summary, we have demonstrated that the CO_2-to-formate performance was improved with reducing dimension of Ru species. We found the $Ru_1@Bi$ exhibited about twofold higher partial current density compared with $Ru_n@Bi$, while over 95% Faradaic efficiency (FE) was maintained. Various electrochemical techniques suggested a balanced adsorption and activation of H_2O and CO_2 molecules on $Ru_1@Bi$. Moreover, ATR-SEIRAS and DFT calculations confirmed the excellent H_2O dissociation and H* migration ability of Ru single atoms, as well as the presence of Ru–Bi bridge sites for accelerated CO_2 hydrogenation. These together enable efficient CO_2-to-formate conversion. Our study provides a mechanistic insight that is important for the designing of high performance electrocatalytic systems, especially for those with hydrogenation as RDS. Future studies can be improved by directly monitor H* spillover using advanced operando spectroscopic methods.

4. Experimental Section

Synthesis of Bi Nanoparticles: For a typical synthesis, 0.5 g of PSS (Poly(sodium 4-styrene-sulfonate), MW = 100 000, Aldrich) and 1 mL of hydrazine hydrate (80% water solution) were dissolved in 50 mL of distilled water. 300 mg of $Bi(NO_3)_3{\cdot}5H_2O$ were added and stirred for 30 min to obtain a white suspension. The suspension was transferred into a teflon-lined stainless steel autoclave with capacity of 100 mL and kept at 160 °C for 6 h. Finally, after centrifugation and being washed with water and ethanol several times, the black powders was collected and dried in a vacuum oven at 60 °C.

Synthesis of Ru@Bi Electrocatalysts: As synthesized Bi nanoparticles (100 mg) were immersed in 40 mL of dimethyl sulfoxide, the various volume of ruthenium chloride ($RuCl_3$, 10 mg mL^{-1}) solution was then added into the mixture followed by stirring for 24 h at room temperature. Since the Bi^{3+}/Bi redox couple has a lower standard reduction potential (E^0 = 0.31 V) compared with Ru^{3+}/Ru (E^0 = 0.60 V), the galvanic replacement reaction of Bi and Ru^{3+} will take place theoretically.[22] After centrifugation and being washed with water and ethanol, the as-prepared sample was dried under vacuum conditions. The Ru@Bi samples with different Ru loading contents were prepared by adding ruthenium chloride solution with different volume of 1 and 2 mL.

Supporting Information

Supporting Information is available from the Wiley Online Library or from the author.

Acknowledgements

X.L. and C.Z. contributed equally to this work. This study was supported by the Westlake Education Foundation (Grant No. 103506022001), Westlake University-Muyuan Joint Research Institute (Grant No. 206006022007), National Key Research and Development Project (2022YFA1503900), Shenzhen fundamental research funding (JCYJ20210324115809026, JCYJ20200109141216566, JCYJ20220818100212027), Guangdong scientific program with contract no. 2019QN01L057, Key projects of the National Foundation of China (512104-N12403ZJ) and China Postdoctoral Foundation (2023M733021). The authors thank Westlake University Instrumentation and Service Center for Physical Sciences, and Molecular Sciences for the facility support and technical assistance. The authors thank the beamline 1W1B of the Beijing Synchrotron Radiation Facility (BSRF) and BL14W1 station of Shanghai Synchrotron Radiation Facility (SSRF) and measurement for providing beam time to support this project.

Conflict of Interest

The authors declare no conflict of interest.

Data Availability Statement

The data that support the findings of this study are available in the supplementary material of this article.

Keywords

atomic species, CO_2 reduction, hydrogen spillover, in situ FT-IR, regulating water dissociation

Received: April 5, 2024
Revised: May 7, 2024
Published online: June 8, 2024

---

[1] a) Y. J. Sa, C. W. Lee, S. Y. Lee, J. Na, U. Lee, Y. J. Hwang, *Chem. Soc. Rev.* **2020**, *49*, 6632; b) D. U. Nielsen, X.-M. Hu, K. Daasbjerg, T. Skrydstrup, *Nat. Catal.* **2018**, *1*, 244; c) C. A. Trickett, A. Helal, B. A. Al-Maythalony, Z. H. Yamani, K. E. Cordova, O. M. Yaghi, *Nat. Rev. Mater.* **2017**, *2*, 17045.
[2] X. Lu, D. Y. C. Leung, H. Wang, M. K. H. Leung, J. Xuan, *ChemElectroChem.* **2014**, *1*, 836.
[3] H. Li, H. Opgenorth Paul, G. Wernick David, S. Rogers, T.-Y. Wu, W. Higashide, P. Malati, Y.-X. Huo, M. Cho Kwang, C. Liao James, *Science.* **2012**, *335*, 1596.

[4] a) C. Lin, Z. Xu, X. Kong, H. Zheng, Z. Geng, J. Zeng, *ChemNanoMat.* **2022**, *8*, 202200020; b) Y. Xing, X. Kong, X. Guo, Y. Liu, Q. Li, Y. Zhang, Y. Sheng, X. Yang, Z. Geng, J. Zeng, *Adv. Sci.* **2020**, *7*, 1902989; c) L. Han, X. Peng, H.-T. Wang, P. Ou, Y. Mi, C.-W. Pao, J. Zhou, J. Wang, X. Liu, W.-F. Pong, J. Song, Z. Lin, J. Luo, H. L. Xin, *Proc. Natl. Acad. Sci.* **2022**, *119*, 2207326119.

[5] a) A. Zhang, Y. Liang, H. Li, B. Zhang, Z. Liu, Q. Chang, H. Zhang, C.-F. Zhu, Z. Geng, W. Zhu, J. Zeng, *Nano Lett.* **2020**, *20*, 8229; b) B. Jia, Z. Chen, C. Li, Z. Li, X. Zhou, T. Wang, W. Yang, L. Sun, B. Zhang, *J. Am. Chem. Soc.* **2023**, *145*, 14101.

[6] a) N. Han, Y. Wang, H. Yang, J. Deng, J. Wu, Y. Li, Y. Li, *Nat. Commun.* **2018**, *9*, 1320; b) S. Liu, X. F. Lu, J. Xiao, X. Wang, X. W. Lou, *Angew. Chem., Int. Ed.* **2019**, *58*, 13828; c) P. Deng, H. Wang, R. Qi, J. Zhu, S. Chen, F. Yang, L. Zhou, K. Qi, H. Liu, B. Y. Xia, *ACS Catal.* **2020**, *10*, 743.

[7] a) H. Xie, T. Zhang, R. Xie, Z. Hou, X. Ji, Y. Pang, S. Chen, M. M. Titirici, H. Weng, G. Chai, *Adv. Mater.* **2021**, *33*, 2008373; b) W. Zhang, S. Yang, M. Jiang, Y. Hu, C. Hu, X. Zhang, Z. Jin, *Nano Lett.* **2021**, *21*, 2650; c) L. Lin, X. He, X.-G. Zhang, W. Ma, B. Zhang, D. Wei, S. Xie, Q. Zhang, X. Yi, Y. Wang, *Angew. Chem., Int. Ed.* **2022**, *62*, 202214959.

[8] a) S. Kim, W. J. Dong, S. Gim, W. Sohn, J. Y. Park, C. J. Yoo, H. W. Jang, J.-L. Lee, *Nano Energy.* **2017**, *39*, 44; b) J. H. Koh, D. H. Won, T. Eom, N.-K. Kim, K. D. Jung, H. Kim, Y. J. Hwang, B. K. Min, *ACS Catal.* **2017**, *7*, 5071; c) Z. Chen, K. Mou, X. Wang, L. Liu, *Angew. Chem., Int. Ed.* **2018**, *57*, 12790; d) F. P. García de Arquer, O. S. Bushuyev, P. De Luna, C.-T. Dinh, A. Seifitokaldani, M. I. Saidaminov, C.-S. Tan, L. N. Quan, A. Proppe, M. G. Kibria, S. O. Kelley, D. Sinton, E. H. Sargent, *Adv. Mater.* **2018**, *30*, 1802858.

[9] a) W. Ma, S. Xie, X.-G. Zhang, F. Sun, J. Kang, Z. Jiang, Q. Zhang, D.-Y. Wu, Y. Wang, *Nat. Commun.* **2019**, *10*, 892; b) J. H. Zhou, K. Yuan, L. Zhou, Y. Guo, M. Y. Luo, X. Y. Guo, Q. Y. Meng, Y. W. Zhang, *Angew. Chem., Int. Ed.* **2019**, *58*, 14197.

[10] J. Greeley, T. F. Jaramillo, J. Bonde, I. Chorkendorff, J. K. Nørskov, *Nat. Mater.* **2006**, *5*, 909.

[11] X. Guo, S.-M. Xu, H. Zhou, Y. Ren, R. Ge, M. Xu, L. Zheng, X. Kong, M. Shao, Z. Li, H. Duan, *ACS Catal.* **2022**, *12*, 10551.

[12] Y. Yang, Y. Yu, J. Li, Q. Chen, Y. Du, P. Rao, R. Li, C. Jia, Z. Kang, P. Deng, Y. Shen, X. Tian, *Nano-Micro Lett.* **2021**, *13*, 160.

[13] Y. Qiao, W. Lai, K. Huang, T. Yu, Q. Wang, L. Gao, Z. Yang, Z. Ma, T. Sun, M. Liu, C. Lian, H. Huang, *ACS Catal.* **2022**, *12*, 2357.

[14] a) M. Nishijima, M. Matsuura, Y. Zhang, A. Makino, *Philos. Mag. Lett.* **2015**, *95*, 277; b) D. K. Pattadar, R. A. Masitas, C. D. Stachurski, D. E. Cliffel, F. P. Zamborini, *J. Am. Chem. Soc.* **2020**, *142*, 19268.

[15] Y. Yao, S. Hu, W. Chen, Z.-Q. Huang, W. Wei, T. Yao, R. Liu, K. Zang, X. Wang, G. Wu, W. Yuan, T. Yuan, B. Zhu, W. Liu, Z. Li, D. He, Z. Xue, Y. Wang, X. Zheng, J. Dong, C.-R. Chang, Y. Chen, X. Hong, J. Luo, S. Wei, W.-X. Li, P. Strasser, Y. Wu, Y. Li, *Nat. Catal.* **2019**, *2*, 304.

[16] H. Liu, X. Lang, C. Zhu, J. Timoshenko, M. Rüscher, L. Bai, N. Guijarro, H. Yin, Y. Peng, J. Li, Z. Liu, W. Wang, B. R. Cuenya, J. Luo, *Angew. Chem., Int. Ed.* **2022**, *61*, 202202556.

[17] G. V. Buxton, C. L. Greenstock, W. P. Helman, A. B. Ross, *J. Phys. Chem. Ref. Data.* **1988**, *17*, 513.

[18] N. Gupta, M. Gattrell, B. Macdougall, *J. Appl. Electrochem.* **2006**, *36*, 161.

[19] a) X.-Y. Ma, W.-Y. Zhang, K. Ye, K. Jiang, W.-B. Cai, *Anal. Chem.* **2022**, *94*, 11337; b) J. Wu, X. Li, W. Shi, P. Ling, Y. Sun, X. Jiao, S. Gao, L. Liang, J. Xu, W. Yan, C. Wang, Y. Xie, *Angew. Chem., Int. Ed.* **2018**, *57*, 8719; c) G. Kumari, X. Zhang, D. Devasia, J. Heo, P. K. Jain, *ACS Nano.* **2018**, *12*, 8330.

[20] S. Chen, X. Li, C.-W. Kao, T. Luo, K. Chen, J. Fu, C. Ma, H. Li, M. Li, T.-S. Chan, M. Liu, *Angew. Chem., Int. Ed.* **2022**, *61*, 202206233.

[21] L. Zhang, X. Yang, Q. Yuan, Z. Wei, J. Ding, T. Chu, C. Rong, Q. Zhang, Z. Ye, F.-Z. Xuan, Y. Zhai, B. Zhang, X. Yang, *Nat. Commun.* **2023**, *14*, 8311.

[22] R. T. Hannagan, G. Giannakakis, M. Flytzani-Stephanopoulos, E. C. H. Sykes, *Chem. Rev.* **2020**, *120*, 12044.